


Cite this: *Energy Adv.*, 2024,  
3, 2758Received 3rd July 2024,  
Accepted 13th September 2024

DOI: 10.1039/d4ya00441h

rsc.li/energy-advances

## Investigating the ion conductivity and synthesis conditions of calcium monocarborane solid-state electrolytes†

Takara Shinohara,<sup>a</sup> Kazuaki Kisu,<sup>b</sup> \*<sup>ab</sup> Shigeyuki Takagi<sup>a</sup> and Shin-ichi Orimo\*<sup>ac</sup>

Multivalent-ion and all-solid-state batteries have emerged as potential solutions to address resource concerns and safety issues. Calcium is a promising element for multivalent-ion batteries owing to its abundance in the Earth's crust and low reduction potential. In addition, complex hydrides exhibit both high ion conductivity and reduction stability, making them suitable materials for solid-state ion conductors. In this study, we investigated the thermal stability and optimised the synthesis conditions of calcium monocarborane, namely,  $\text{Ca}(\text{CB}_{11}\text{H}_{12})_2$ , which is a *closo*-type calcium complex hydride. In addition, we conducted electrochemical analysis to assess its performance as a solid-state divalent-ion conductor. The results indicate that a heat-treatment temperature of 433 K provides  $\text{Ca}(\text{CB}_{11}\text{H}_{12})_2$  with higher ion conductivity ( $\sigma = 1.42 \times 10^{-4} \text{ S cm}^{-1}$ ) than the other heating temperatures. Thus, 433 K is considered optimal because  $[\text{CB}_{11}\text{H}_{12}]^-$  anions decompose when heat-treated at and above 453 K. Furthermore, the insertion and deinsertion of  $\text{Ca}^{2+}$  ions are stable and reversible in symmetric cells employing Ca–Sn alloy electrodes, representing the first time this has been observed for an inorganic solid-state calcium-ion conductor. Such insertion and deinsertion highlight the potential of  $\text{Ca}(\text{CB}_{11}\text{H}_{12})_2$  as a solid-state electrolyte for battery applications.

Lithium-ion batteries (LiBs) are primarily used in portable devices and electric vehicles. However, LiBs pose safety concerns because of their flammable organic solvents and the risk of short-circuiting caused by dendritic Li growth. Ongoing developments in the fields of all-solid-state and multivalent-ion batteries aim to address these issues.

Inorganic solid-state ion conductors play a crucial role in all-solid-state batteries because of their safety and electrochemical properties.<sup>1–4</sup> Replacing flammable liquid electrolytes with non-flammable inorganic solid-state ion conductors enhances battery safety.<sup>5</sup> Moreover, inorganic solid-state ion conductors consist of robust solids; therefore, they prevent the dendritic growth that occurs during the charging process with lithium-metal anodes and causes short-circuiting.<sup>5</sup>

Inorganic solid-state ion conductors offer several advantages in terms of electrochemical properties. Compared with liquid electrolytes, they exhibit excellent performance across a broader temperature range because of their high thermal stability.<sup>6</sup> In addition, solid electrolytes have a high transference number ( $\sim 1$ ),<sup>7–9</sup> indicating that the undesired concentration polarisation observed in liquid electrolytes does not occur. Furthermore, some inorganic solid electrolytes exhibit a wide potential window.<sup>10,11</sup>

Types of inorganic ion conductors include sulphide, oxide, and complex-hydride solid electrolytes. Notably, complex hydrides have attracted attention as solid ion conductors for several reasons: (i) their wide potential window enables their use with metal electrodes with large specific capacities. (ii) their deformability facilitates the formation of excellent electrode/electrolyte interfaces. (iii) their low density enables the fabrication of lightweight devices.<sup>12,13</sup>

Complex hydrides, typically denoted as  $\text{M}_x(\text{M}'_y\text{H}_z)$  (where M is a metal cation and  $\text{M}'_y\text{H}_z$  is a complex anion), have been studied as solid-state ion conductors because  $\text{LiBH}_4$ <sup>14</sup> exhibits superionic conduction at high temperatures.<sup>15–17</sup> Notably, *closo*-type complex hydrides containing large cage-like anions have been reported to exhibit exceptionally high ion conductivity<sup>18–22</sup> and maintain this high conductivity at room temperature.<sup>23,24</sup>

Complex hydrides containing multivalent cations have attracted significant interest.<sup>25–28</sup> Multivalent metals, such as magnesium, calcium, and aluminium, offer a resource advantage because of their abundance in the Earth's crust.<sup>29</sup> Furthermore, multivalent-ion conductors typically possess two to three

<sup>a</sup> Institute for Materials Research (IMR), Tohoku University, Katahira 2-1-1, Aoba-ku, Sendai 980-8577, Japan. E-mail: [kkisu@shibaura-it.ac.jp](mailto:kkisu@shibaura-it.ac.jp), [shin-ichi.orimo.a6@tohoku.ac.jp](mailto:shin-ichi.orimo.a6@tohoku.ac.jp)

<sup>b</sup> College of Engineering, Shibaura Institute of Technology, Toyosu 3-7-5 Koto-ku, Tokyo 135-8548, Japan

<sup>c</sup> Advanced Institute for Materials Research (WPI-AIMR), Tohoku University, Katahira 2-1-1, Aoba-ku, Sendai 980-8577, Japan

† Electronic supplementary information (ESI) available. See DOI: <https://doi.org/10.1039/d4ya00441h>



times the number of mobile electrons compared to monovalent-ion conductors.<sup>30</sup> Consequently, multivalent-ion complex hydrides have been investigated to determine whether they can function as liquid electrolytes or solid-state ion conductors.<sup>31–34</sup> Furthermore, *closo*-type complex hydrides containing multivalent cations exhibit excellent electrochemical properties.<sup>35–38</sup>

Calcium shows immense promise as a metal anode because of its greater abundance<sup>29,39,40</sup> in the Earth's crust and lower redox potential ( $-2.87$  V vs. SHE) compared to magnesium ( $-2.37$  V vs. SHE) and zinc ( $-0.76$  V vs. SHE).<sup>29,41</sup> Furthermore, its low polarisation and charge density suggest that ion conduction in the solid state may be faster than that of magnesium and zinc.<sup>42,43</sup> Therefore, liquid electrolytes for rechargeable calcium batteries have been investigated.<sup>42,44–47</sup> However, dendritic growth was observed in a  $\text{Ca}(\text{BH}_4)_2/\text{THF}$  liquid electrolyte with high Coulombic efficiency (94.8%).<sup>47,48</sup> To suppress dendritic growth, solid electrolytes must be used for rechargeable calcium batteries. Consequently, *closo*-type complex hydrides containing calcium cations are expected to exhibit excellent properties as solid-state ion conductors. Calcium monocarbaborane (CMC,  $\text{Ca}(\text{CB}_{11}\text{H}_{12})_2$ ) is a *closo*-type complex hydride containing one calcium cation and two monocarbaborane anions. Besides CMC, lithium<sup>21–23,49,50</sup> and sodium<sup>21,22,49–51</sup> monocarbaborane have also been investigated as solid electrolytes. CMC has been studied as a liquid electrolyte<sup>44</sup> and hydrate;<sup>38</sup> however, research on its performance as a solid-state ion conductor has been limited, particularly regarding its ion conductivity at various temperatures. In addition, electrode reactions that involve  $\text{Ca}^{2+}$  insertion and deinsertion through solids have not been reported previously.

In this study, we optimised the heat-treatment conditions of CMC as a solid-state ion conductor using  $^1\text{H}$  and  $^{11}\text{B}$  nuclear

magnetic resonance (NMR), Raman, and electrochemical impedance spectroscopy (EIS). Furthermore, galvanostatic measurements were conducted using the Ca–Sn alloy as the electrode to identify the conducting ions in CMC.

An X-ray diffraction analysis was conducted to confirm the presence of impurities in the synthesised material. The results show that the synthesised hydrated CMC does not contain the  $\text{CsCB}_{11}\text{H}_{12}$  salt used as the starting material or the  $\text{CaCO}_3$  used for neutralisation (Fig. S1, ESI<sup>†</sup>). This indicates that impurities were not present in the synthesised material.

To investigate the appearance of the CMC powders and identify their composition, observations and analyses were performed using scanning electron microscopy-energy-dispersive X-ray spectroscopy (SEM-EDS). The SEM image reveals that the CMC powders consist of primary particles approximately  $1\ \mu\text{m}$  in size, with the secondary particles formed from them ranging from 2 to  $10\ \mu\text{m}$  in size (Fig. 1a). The primary particles exhibit exceptionally smooth edges. This feature was also confirmed in a previous study on  $0.7\text{LiCB}_9\text{H}_{10}-0.3\text{LiCB}_{11}\text{H}_{12}$ <sup>23</sup> and is consistent with the highly deformable nature of general complex hydrides. The EDS analysis confirmed the uniform presence of boron, carbon, and calcium in the CMC powders. To evaluate the deformability of the CMC powders, they were pressed and moulded into pellet form. The appearance of the pellet (Fig. S2, ESI<sup>†</sup>) suggests that CMC exhibits high deformability, similar to other complex hydrides.

To investigate the thermal stability of CMC, heat treatments were conducted at various temperatures. Our previous research indicated that  $433\ \text{K}$  is the lowest temperature at which dehydration is completed.<sup>44</sup> Therefore, CMC was heat-treated at  $433$ ,  $453$ ,  $473$ , and  $513\ \text{K}$ , which are referred to as CMC (433), (453), (473), and (513), respectively. Raman spectroscopy was

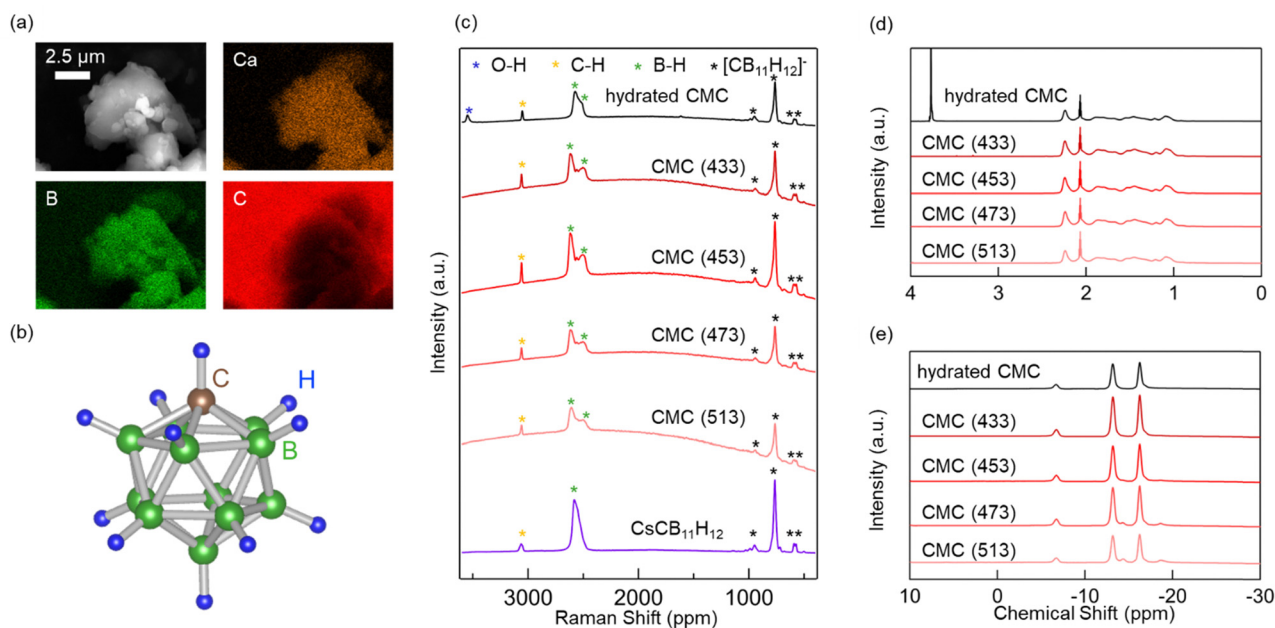


**Fig. 1** (a) SEM image and EDS analysis of CMC particles. (b) Molecular model of  $[\text{CB}_{11}\text{H}_{12}]^-$  anion. (c) Raman spectra of  $\text{CsCB}_{11}\text{H}_{12}$ , hydrated CMC, and CMC heat-treated at different temperatures ( $T = 433, 453, 473,$  and  $513\ \text{K}$ ). (d)  $^1\text{H}$  and (e)  $^{11}\text{B}$  NMR spectra of hydrated CMC and CMC (433–513 K).



conducted to confirm the presence of  $[\text{CB}_{11}\text{H}_{12}]^-$  anions and investigate the thermal stability of CMC. The structure of the  $[\text{CB}_{11}\text{H}_{12}]^-$  anion is icosahedral, with 11 boron atoms and one carbon vertex (Fig. 1b). Peaks derived from the  $[\text{CB}_{11}\text{H}_{12}]^-$  anions were detected in the range of 500–1000  $\text{cm}^{-1}$  for all the samples (Fig. 1c).<sup>23,44,52</sup> In the unheated sample (hydrated CMC), a peak corresponding to  $\text{H}_2\text{O}$  molecules was observed at approximately 3500  $\text{cm}^{-1}$ . However, this peak was not present in any of the heat-treated samples (CMC (433–513)).

$^1\text{H}$  and  $^{11}\text{B}$  NMR spectroscopy were also performed. The  $^1\text{H}$  NMR results revealed a peak at 3.8 ppm, indicating the presence of  $-\text{OH}$  groups in the unheated sample, whereas this peak was absent in all samples heated at and above 433 K (Fig. 1d). This suggests that the  $\text{H}_2\text{O}$  molecules coordinated to CMC were not removed until the heat treatment, which is consistent with the Raman spectroscopy results. The  $^{11}\text{B}$  NMR results of all the samples showed peaks at  $-13$  and  $-16$  ppm corresponding to  $[\text{CB}_{11}\text{H}_{12}]^-$  anions (Fig. 1e).<sup>53</sup> However, different peaks appeared at  $-14$  and  $-18$  ppm in the samples heated at and above 453 K (CMC(453–513)), indicating that  $[\text{CB}_{11}\text{H}_{12}]^-$  anions partially decomposed at and above 453 K. Berger *et al.* investigated the thermal stability of CMC-1.9 $\text{H}_2\text{O}$  under an argon atmosphere. Their study confirmed that decomposition was accompanied by hydrogen gas emission at 448 and 468 K.<sup>38</sup> Thus, anhydrous CMC may have decomposed along with the generation of hydrogen gas at the higher temperatures in the present study.

EIS was conducted to assess the electrical conductivity of the symmetric Au/CMC (433–513)/Au cell. In the Nyquist plot (Fig. S3a, ESI<sup>†</sup>), the semicircle corresponding to electric conduction does not appear at room temperature for any of the samples. Only a portion of the large semicircle is visible within the frequency range of the EIS data because all the samples have exceptionally high electrical resistance. The Nyquist plot (Fig. S3b, ESI<sup>†</sup>) shows semicircles for all the samples,

indicating that they are all electrically conductive at 373 K. The Nyquist plot recorded at 423 K in Fig. 2a shows one semicircle in the high-frequency range and one spike in the low-frequency range, which correspond to contributions from the bulk/grain boundary resistance and interfacial capacity, respectively. In previous studies,<sup>23,54</sup> *closo*-type complex-hydride solid-state ion conductors exhibited bulk/grain boundary resistance. In addition, the CMC (433) plot exhibits a smaller semicircle than the other samples, which means that its electrical conductivity is the highest. For the other samples, the lower electrical conductivity may have been due to the partial decomposition of  $[\text{CB}_{11}\text{H}_{12}]^-$  anions. While the resistance of CMC (513) appears to be significantly large at the scale of the Nyquist plot (Fig. 2a), this value is reasonable considering the relationship between the heat-treatment temperature and resistance of CMC (Fig. S4, ESI<sup>†</sup>). Therefore, these results suggest that electrical conductivity was optimised by heat treatment at 433 K.

The cyclic voltammetry (CV) results described below indicates that CMC is a calcium-ion conductor. The Arrhenius plots of all samples in the 303–423 K temperature range are shown in Fig. 2b. For comparison, the Arrhenius plots of hydrated CMC<sup>38</sup> are also shown in the same figure. Ionic conductivity increased with increasing temperature. As mentioned above, CMC (433) exhibited high ionic conductivity ( $\sigma = 1.42 \times 10^{-4} \text{ S cm}^{-1}$ ) at 423 K. This value surpasses that of previously reported calcium-ion conductors<sup>55,56</sup> at relatively low temperatures. This enhancement can be attributed to the lattice created by the large cage-like  $[\text{CB}_{11}\text{H}_{12}]^-$  anions, which favours cation conduction.<sup>22</sup> The Arrhenius plot of CMC (433) in the first heating process (Fig. S5a, ESI<sup>†</sup>) shows that the slope changed at approximately 383 K. To investigate this change in slope, differential thermal analysis (DTA) was conducted, which revealed a slightly endothermic peak at approximately 393–403 K (Fig. S6, ESI<sup>†</sup>). The appearance of this endothermic peak can be attributed to a change in the activation energy for charge

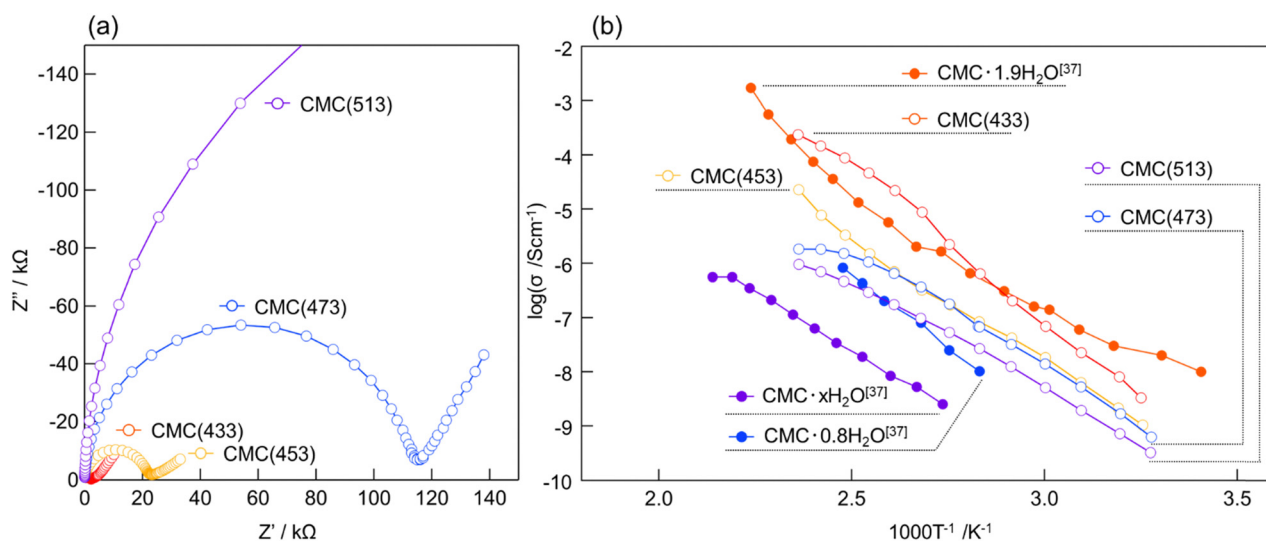


Fig. 2 (a) Nyquist plots at 423 K of CMC heat-treated at different temperatures ( $T = 433, 453, 473,$  and  $513$  K). (b) Arrhenius plots of CMC (433–513) and hydrated CMCs.<sup>37</sup>



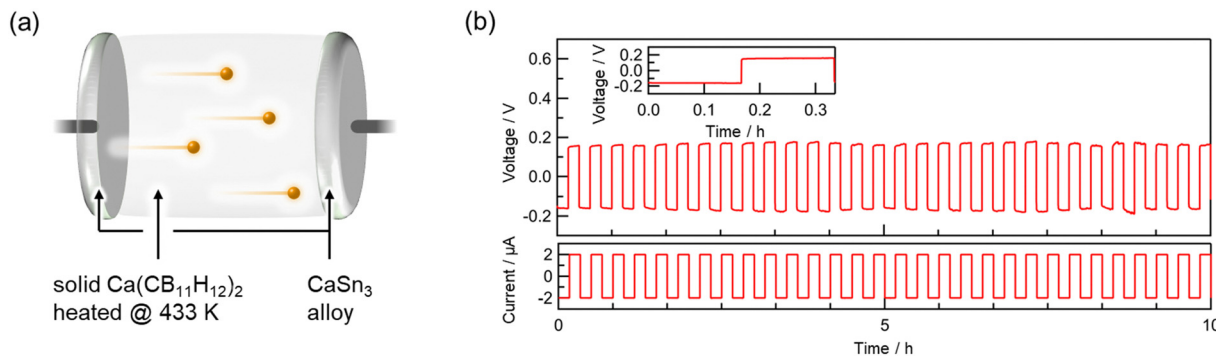


Fig. 3 (a) Illustration of symmetric cell setup (CaSn<sub>3</sub> alloy|CMC heated at 433 K). (b) Voltage response (top), applied current, and voltage response for 0–20 min (inset) in galvanostatic test using CaSn<sub>3</sub> symmetric cell.

transfer caused by the structural phase transition, which is a phenomenon commonly observed in complex hydrides.<sup>14,24</sup> The change in the slope of the Arrhenius plot during cooling was relatively slow compared to that during the heating process (Fig. 2b and Fig. S5, ESI†). The DTA results showed no exothermic peaks during the cooling process, suggesting that a gradual phase transition occurred from a high-temperature phase to a low-temperature phase (Fig. S5a and b, ESI†). The difference in the rate of temperature change explains the discrepancy between the change in the slope of the Arrhenius plot and the temperature at which the DTA endothermic peak was observed. CMC might exhibit a high-temperature phase with high ionic conductivity, similar to other complex hydrides, and is believed to undergo a phase transition to this state at high temperatures. CMC (433) has an activation energy of 77.9 kJ mol<sup>-1</sup> at the high-temperature phase. Although the activation energy of hydrated CMC was not reported in a previous paper,<sup>38</sup> the fact that there is almost no difference between the slopes of the Arrhenius plots of CMC and hydrated CMC indicates that this value is reasonable. In addition, this value is of a similar order of magnitude to those of reported solid-state calcium-ion conductors (146 kJ mol<sup>-1</sup> for Ca<sub>0.5</sub>Zr<sub>2</sub>(PO<sub>4</sub>)<sub>3</sub><sup>55</sup> and 55.8 kJ mol<sup>-1</sup> for (Ca<sub>0.05</sub>Hf<sub>0.95</sub>)<sub>4/3.9</sub>Nb(PO<sub>4</sub>)<sub>3</sub><sup>56</sup>).

To investigate suitable anode materials for CMC, CV was performed using calcium metal and a Ca–Sn alloy. Ca–Sn alloys have been reported as active anode materials in calcium-ion batteries.<sup>57</sup> A mixture of CaSn<sub>3</sub>, Ketjen black, and CMC (433) was used as the composite electrode. A CaSn<sub>3</sub>|CMC|CaSn<sub>3</sub> pellet was prepared for the CV measurements (Fig. S7, ESI†). The CaSn<sub>3</sub> composite electrode did not peel off from the CMC pellet. The prepared pellet was split into two, and the cross section was observed using SEM-EDS (Fig. S8a, ESI†). EDS elemental mapping analysis indicated that the particles in the Ca–Sn composite electrode layer were Ca–Sn alloy (Fig. S8b–e, ESI†). These particles were mixed in the CMC electrolyte layer and made the interface adhesive, indicating that sufficient electrode/electrolyte interface was formed to cause an alloying/dealloying reaction. The CV curve recorded at 423 K using Ca metal showed a small current response to the applied voltage (Fig. S9a, ESI†). This low current value is similar to that of a symmetric cell using Mo foil electrodes (Fig. S9b, ESI†), in which

only electrons are transferred. Limited charge transfer occurred without calcium plating/stripping likely because of the instability of CMC against calcium metal owing to the high reactivity between them at high temperature. In contrast, a relatively large increase in current response was observed when applying a constant voltage ( $E = \pm 1$  V vs. Ca–Sn alloy) in the CV curve using the Ca–Sn alloy (Fig. S9c, ESI†). This can likely be attributed to the charge transfer associated with the insertion–deinsertion reaction, which in this case means the alloying–dealloying process in which Ca<sup>2+</sup> ions diffuse in CMC and react reversibly with the Ca–Sn alloy.

To investigate the electrochemical stability of this alloying dealloying reaction, a galvanostatic test was conducted using the Ca–Sn alloy. The symmetric electrochemical cell for the galvanostatic test was assembled with a CMC (433) pellet sandwiched between the composite electrodes (Fig. 3a). The voltage response immediately followed the applied current of 2  $\mu$ A (Fig. 3b inset). This suggests that an alloying–dealloying reaction proceeded between CMC and the Ca–Sn alloy with a relatively low overvoltage. The stability of the CMC in the Ca–Sn alloy was evaluated by repeatedly applying a constant current. The voltage response exhibited a symmetrical square wave, similar to the applied current. This indicates that CMC exhibited stable behaviour against the Ca–Sn alloy at 423 K. An alloying–dealloying reaction using a solid electrolyte was thus confirmed for the first time for an inorganic solid-state calcium-ion conductor, highlighting the potential of Ca(CB<sub>11</sub>H<sub>12</sub>)<sub>2</sub> as a solid-state electrolyte for battery applications.

## Conclusions

We optimised the heat treatment conditions for CMC, which is a *closo*-type complex hydride. Raman spectroscopy and <sup>1</sup>H and <sup>11</sup>B NMR results indicate that at a thermal treatment temperature of 433 K, the coordinated water molecules are completely removed and the [CB<sub>11</sub>H<sub>12</sub>]<sup>-</sup> anions do not decompose. Furthermore, electrochemical tests, EIS, and CV tests show that CMC heat-treated at 433 K exhibits high ion conductivity ( $\sigma = 1.42 \times 10^{-4}$  S cm<sup>-1</sup>) at 423 K. The solid-state cells using CMC exhibit a stable and reversible alloying–dealloying property with a Ca–Sn alloy electrode during the galvanostatic test, suggesting



the availability of CMC as a solid-state electrolyte. The Arrhenius plots and DTA results suggest that CMC heat-treated at 433 K may undergo a structural phase transition at approximately 383–403 K.

## Author contributions

K. K. conceived and designed the study. T. S. performed the synthesis, measurements, and data analysis. K. K. performed the NMR measurements. K. K., S. T., and S. O. discussed the results. T. S. wrote the manuscript. K. K. and S. O. supervised the study. All authors discussed and commented on the manuscript.

## Data availability

The data supporting this article have been included as part of the ESI.†

## Conflicts of interest

There are no conflicts to declare.

## Acknowledgements

This work was supported by a JSPS KAKENHI Grant-in-Aid for Scientific Research B (No. 22H01803) and a Grant-in-Aid for Scientific Research on Innovative Areas (“Hydrogenomics”, No. 18H05513). It was also supported by the Shiraiishi foundation of science development. We thank H. Ohmiya and N. Warifune of Tohoku University for their technical assistance.

## References

- 1 S. Ohno, A. Banik, G. F. Dewald, M. A. Kraft, T. Krauskopf, N. Minafra, P. Till, M. Weiss and W. G. Zeier, *Prog. Energy*, 2020, **2**, 022001.
- 2 Q. Liu, L. Jiang, P. Zheng, J. Sun, C. Liu, J. Chai, X. Li, Y. Zheng and Z. Liu, *Chem. Rec.*, 2022, **22**, e202200116.
- 3 Y.-C. Jung, S.-K. Kim, M.-S. Kim, J.-H. Lee, M.-S. Han, D.-H. Kim, W.-C. Shin, M. Ue and D.-W. Kim, *J. Power Sources*, 2015, **293**, 675–683.
- 4 R. Chen, Q. Li, X. Yu, L. Chen and H. Li, *Chem. Rev.*, 2020, **120**, 6820–6877.
- 5 J. Janek and W. G. Zeier, *Nat. Energy*, 2016, **1**, 16141.
- 6 Y.-S. Hu, *Nat. Energy*, 2016, **1**, 16042.
- 7 A. Mauger, C. M. Julien, A. Paoletta, M. Armand and K. Zaghib, *Materials*, 2019, **12**, 3892.
- 8 R. Kanno, *Electrochemistry*, 2023, **91**, 102001.
- 9 J. C. Bachman, S. Muy, A. Grimaud, H. H. Chang, N. Pour, S. F. Lux, O. Paschos, F. Maglia, S. Lupart, P. Lamp, L. Giordano and Y. Shao-Horn, *Chem. Rev.*, 2016, **116**, 140–162.
- 10 J. Hassoun, R. Verrelli, P. Reale, S. Panero, G. Mariotto, S. Greenbaum and B. Scrosati, *J. Power Sources*, 2013, **229**, 117–122.
- 11 J. B. Goodenough and Y. Kim, *Chem. Mater.*, 2009, **22**, 587–603.
- 12 R. Mohtadi and S. Orimo, *Nat. Rev. Mater.*, 2017, **2**, 16091.
- 13 F. Cuevas, M. B. Amdisen, M. Baricco, C. E. Buckley, Y. W. Cho, P. de Jongh, L. M. de Kort, J. B. Grinderslev, V. Gulino, B. C. Hauback, M. Heere, T. Humphries, T. R. Jensen, S. Kim, K. Kisu, Y.-S. Lee, H.-W. Li, R. Mohtadi, K. T. Møller, P. Ngene, D. Noréus, S. Orimo, M. Paskevicius, M. Polanski, S. Sartori, L. N. Skov, M. H. Sørby, B. C. Wood, V. A. Yartys, M. Zhu and M. Latroche, *Prog. Energy*, 2022, **4**, 032001.
- 14 M. Matsuo, Y. Nakamori, S. Orimo, H. Maekawa and H. Takamura, *Appl. Phys. Lett.*, 2007, **91**, 224103.
- 15 N. Toyama, S. Kim, H. Oguchi, T. Sato, S. Takagi, M. Tazawa, G. Nogami and S. Orimo, *J. Energy Chem.*, 2019, **38**, 84–87.
- 16 Y. Yan, R. S. Kühnel, A. Remhof, L. Duchêne, E. C. Reyes, D. Rentsch, Z. Łodziana and C. Battaglia, *Adv. Energy Mater.*, 2017, **7**, 1700294.
- 17 A. Unemoto, T. Ikeshoji, S. Yasaku, M. Matsuo, V. Stavila, T. J. Udovic and S. Orimo, *Chem. Mater.*, 2015, **27**, 5407–5416.
- 18 T. A. Hales, K. T. Møller, T. D. Humphries, A. M. D'Angelo, C. E. Buckley and M. Paskevicius, *J. Phys. Chem. C*, 2023, **127**, 949–957.
- 19 D. H. P. Souza, A. M. D'Angelo, T. D. Humphries, C. E. Buckley and M. Paskevicius, *Dalton Trans.*, 2022, **51**, 13848–13857.
- 20 K. Yoshida, T. Sato, A. Unemoto, M. Matsuo, T. Ikeshoji, T. J. Udovic and S. Orimo, *Appl. Phys. Lett.*, 2017, **110**, 103901.
- 21 W. S. Tang, M. Matsuo, H. Wu, V. Stavila, W. Zhou, A. A. Talin, A. V. Soloninin, R. V. Skoryunov, O. A. Babanova, A. V. Skripov, A. Unemoto, S. Orimo and T. J. Udovic, *Adv. Energy Mater.*, 2016, **6**, 1502237.
- 22 W. S. Tang, A. Unemoto, W. Zhou, V. Stavila, M. Matsuo, H. Wu, S. Orimo and T. J. Udovic, *Energy Environ. Sci.*, 2015, **8**, 3637–3645.
- 23 S. Kim, H. Oguchi, N. Toyama, T. Sato, S. Takagi, T. Otomo, D. Arunkumar, N. Kuwata, J. Kawamura and S. Orimo, *Nat. Commun.*, 2019, **10**, 1081.
- 24 S. Kim, K. Kisu, S. Takagi, H. Oguchi and S. Orimo, *ACS Appl. Energy Mater.*, 2020, **3**, 4831–4839.
- 25 Q. Wang, Z. Li, H. Deng, Y. Chen and Y. Yan, *Chem. Commun.*, 2023, **59**, 6726–6729.
- 26 L. G. Kristensen, M. B. Amdisen, L. N. Skov and T. R. Jensen, *Phys. Chem. Chem. Phys.*, 2022, **24**, 18185–18197.
- 27 Y. Yan, W. Dononelli, M. Jørgensen, J. B. Grinderslev, Y. S. Lee, Y. W. Cho, R. Černý, B. Hammer and T. R. Jensen, *Phys. Chem. Chem. Phys.*, 2020, **22**, 9204–9209.
- 28 T. Shinohara, K. Kisu, A. Dorai, K. Zushida, H. Yabu, S. Takagi and S. Orimo, *Adv. Sci.*, 2024, e2308318.
- 29 Q. Liu, H. Wang, C. Jiang and Y. Tang, *Energy Storage Mater.*, 2019, **23**, 566–586.
- 30 K. Kisu, R. Mohtadi and S. Orimo, *Adv. Sci.*, 2023, **10**, 2301178.
- 31 R. Mohtadi, M. Matsui, T. S. Arthur and S. J. Hwang, *Angew. Chem., Int. Ed.*, 2012, **51**, 9780–9783.
- 32 E. Roedern, R. S. Kühnel, A. Remhof and C. Battaglia, *Sci. Rep.*, 2017, **7**, 46189.



- 33 K. Kisu, S. Kim, M. Inukai, H. Oguchi, S. Takagi and S. Orimo, *ACS Appl. Energy Mater.*, 2020, **3**, 3174–3179.
- 34 T. Burankova, E. Roedern, A. E. Maniadaki, H. Hagemann, D. Rentsch, Z. Łodziana, C. Battaglia, A. Remhof and J. P. Embs, *J. Phys. Chem. Lett.*, 2018, **9**, 6450–6455.
- 35 O. Tutusaus, R. Mohtadi, T. S. Arthur, F. Mizuno, E. G. Nelson and Y. V. Sevyugina, *Angew. Chem., Int. Ed.*, 2015, **54**, 7900–7904.
- 36 K. Kisu, A. Dorai, S. Kim, R. Hamada, A. Kumatani, Y. Horiguchi, R. Sato, K. Sau, S. Takagi and S. Orimo, *J. Mater. Chem. A*, 2022, **10**, 24877–24887.
- 37 T. J. Carter, R. Mohtadi, T. S. Arthur, F. Mizuno, R. Zhang, S. Shirai and J. W. Kampf, *Angew. Chem., Int. Ed.*, 2014, **53**, 3173–3177.
- 38 A. Berger, A. Ibrahim, C. E. Buckley and M. Paskevicius, *Phys. Chem. Chem. Phys.*, 2023, **25**, 5758–5775.
- 39 Q. Wei, L. Zhang, X. Sun and T. L. Liu, *Chem. Sci.*, 2022, **13**, 5797–5812.
- 40 L. Yan, W. Yang, H. Yu, L. Zhang and J. Shu, *Energy Storage Mater.*, 2023, **60**, 102822.
- 41 H. Zhao, J. Xu, D. Yin and Y. Du, *Chem. – Eur. J.*, 2018, **24**, 18220–18234.
- 42 A. Ponrouch, C. Frontera, F. Bardé and M. R. Palacín, *Nat. Mater.*, 2016, **15**, 169–172.
- 43 C. Chen, F. Shi and Z.-L. Xu, *J. Mater. Chem. A*, 2021, **9**, 11908–11930.
- 44 K. Kisu, S. Kim, T. Shinohara, K. Zhao, A. Züttel and S. Orimo, *Sci. Rep.*, 2021, **11**, 7563.
- 45 Z. Li, O. Fuhr, M. Fichtner and Z. Zhao-Karger, *Energy Environ. Sci.*, 2019, **12**, 3496–3501.
- 46 S. Biria, S. Pathreker, H. Li and I. D. Hosein, *ACS Appl. Energy Mater.*, 2019, **2**, 7738–7743.
- 47 D. Wang, X. Gao, Y. Chen, L. Jin, C. Kuss and P. G. Bruce, *Nat. Mater.*, 2018, **17**, 16–20.
- 48 S. D. Pu, C. Gong, X. Gao, Z. Ning, S. Yang, J.-J. Marie, B. Liu, R. A. House, G. O. Hartley, J. Luo, P. G. Bruce and A. W. Robertson, *ACS Energy Lett.*, 2020, **5**, 2283–2290.
- 49 J. B. Varley, K. Kweon, P. Mehta, P. Shea, T. W. Heo, T. J. Udovic, V. Stavila and B. C. Wood, *ACS Energy Lett.*, 2016, **2**, 250–255.
- 50 W. S. Tang, K. Yoshida, A. V. Soloninin, R. V. Skoryunov, O. A. Babanova, A. V. Skripov, M. Dimitrievska, V. Stavila, S. Orimo and T. J. Udovic, *ACS Energy Lett.*, 2016, **1**, 659–664.
- 51 V. Gulino, A. Longo, L. M. de Kort, H. P. Rodenburg, F. Murgia, M. Brighi, R. Černý, C. J. Sahle, M. Sundermann, H. Gretarsson, F. de Groot and P. Ngene, *Small Methods*, 2024, **8**, e2300833.
- 52 D. Sethio, L. M. L. Daku and H. Hagemann, *Int. J. Hydrogen Energy*, 2017, **42**, 22496–22501.
- 53 S. Körbe, P. J. Schreiber and J. Michl, *Chem. Rev.*, 2006, **106**, 5208–5249.
- 54 T. J. Udovic, M. Matsuo, A. Unemoto, N. Verdal, V. Stavila, A. V. Skripov, J. J. Rush, H. Takamura and S. Orimo, *Chem. Commun.*, 2014, **50**, 3750–3752.
- 55 K. Nomura, S. Ikeda, K. Ito and H. Einaga, *Bull. Chem. Soc. Jpn.*, 1992, **65**, 3221–3227.
- 56 W. Lee, S. Tamura and N. Imanaka, *Chem. Lett.*, 2017, **46**, 1486–1489.
- 57 Z. Zhao-Karger, Y. Xiu, Z. Li, A. Reupert, T. Smok and M. Fichtner, *Nat. Commun.*, 2022, **13**, 3849.

